Chapter 3. High-Frequency (>100 GHz) and High-Speed (<10 ps) Electronic Devices

Academic and Research Staff

Professor Qing Hu, Dr. Gerhard de Lange, Dr. Simon Verghese

Graduate Students

Erik Duerr, Ilya Lyubomirsky, Arifur Rahman, Farhan Rana, Rolf A. Wyss, Bin Xu, Noah D. Zamdmer

3.1 Introduction

Millimeter-wave and far-infrared frequencies (f > 100 GHz) remain one of the most underdeveloped frequency ranges, even though there are great numbers of potential applications in remote sensing, spectroscopy, plasma diagnostics, and communications. This is because the millimeter wave and far-infrared frequency range falls between two other frequency ranges in which conventional semiconductor devices are usually operated, the microwave frequency range and the near-infrared and optical frequency range. Semiconductor devices which utilize the classical diffusive transport of electrons, such as diodes and transistors, have a high frequency limit. This limit is set by the time electrons take to travel a certain distance. Currently, electron mobility and the smallest feature size which can be fabricated by lithography limit the frequency range to below several hundred GHz. Semiconductor devices based on quantum mechanical interband transitions, however, are limited to frequencies higher than those corresponding to the semiconductor energy gap, which is higher than 10 THz for most bulk semiconductors. Therefore, a large gap exists from 100 GHz to 10 THz in which very few devices are available.

Semiconductor quantum-effect devices (which can be loosely termed "artificial atoms"), including both vertically grown quantum-well structures and laterally confined mesoscopic devices, are human-made quantum mechanical systems in which the energy levels can be chosen by changing the sizes of the devices. Typically, the frequency corresponding to the intersubband transitions is in the millimeter-wave to THz range ($\Delta E \sim$ 1-4 meV) for the lateral quantum-effective devices, and above one THz for the vertical quantum wells. It is therefore appealing to develop ultrahigh-frequency devices, such as radiation detectors and mixers, THz lasers, and parametric frequency down converters utilizing the intersubband transitions in these devices. Furthermore, the study of the interaction between photons (with energies comparable to the intersubband spacings) and the quantum-effect devices (artificial atoms) is analogous to optical spectroscopy in atomic physics. Naturally, this study will literally shine "new light" on these devices, and new information can be obtained that cannot be extracted from dc transport measurements. It is also clear that devices with THz characteristic frequencies will have picosecond speed response. Such ultrahigh-speed devices could be useful in easing the electronic "bottleneck" in the current fiber optical communication systems, in which only a small fraction of the 20-THz bandwidth of optical fibers are utilized because of the slow speed of electronic devices.

In addition to new physical concepts, novel technologies must also be developed to meet the challenges at these high frequencies. Conventional mechanically machined horn antennas integrated with waveguide cavities have been the workhorse at microwave and millimeter-wave frequencies since they were first implemented more than 50 years ago during World War II. Very high antenna gain and essentially perfect antenna efficiency can be achieved using these structures. However, they are expensive, bulky, and incompatible with arrays. In order to overcome these problems, there have been new developments in micromachining to fabricate the horn antenna structures. In these structures, the active elements and their planar antennas are fabricated on a free-standing thin (~1 micron) SiN membrane, which is suspended over a silicon pyramidal horn that is formed by anisotropic etching or micromachining. The side walls of this micromachined structure can then be coated with Au to form a horn antenna. Compared to conventional waveguide horn antennas, this micromachined structure has several major advantages. It is easier to fabricate fine three-dimensional structures by using photolithography. Horn antennas with micron precision can be easily defined and inexpensively mass produced. They are made on Si or GaAs wafers and compatible with thin-film technology. Thus, active elements, such as RF and IF amplifiers, mixers and video detectors, local oscillators, and post-detection signal processors, can be integrated monolithically with the antenna structures to form

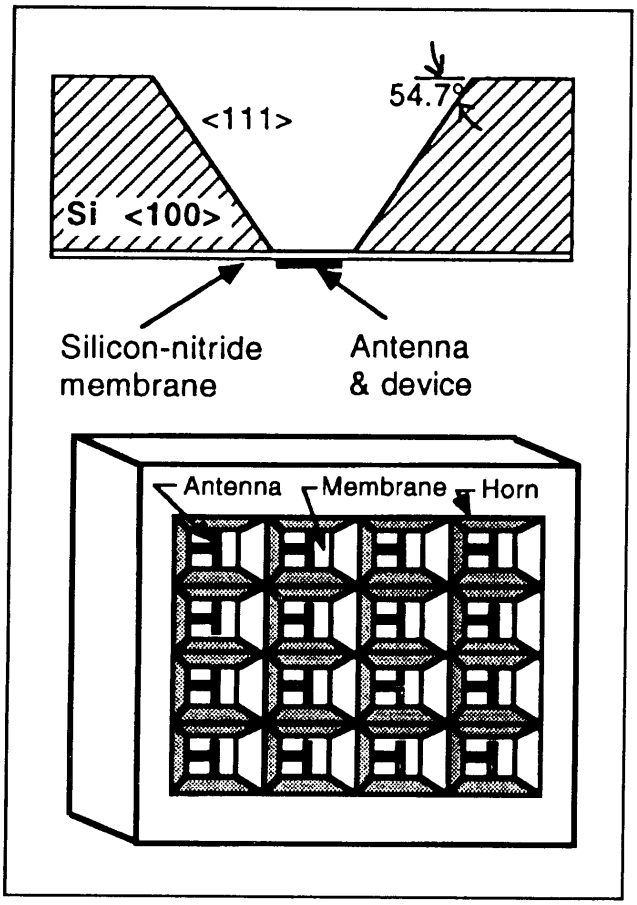

Figure 1. (a)(top) Example of a micromachined horn antenna structure that is made by anisotropically etching a <100> silicon wafer. (b)(bottom) Schematic of a focal-plane array on a single wafer made using micromachining.

monolithic transmitter/receiver systems which are light-weight and compact. The most attractive feature of the micromachined structure is that focal-plane arrays can be fabricated easily on a single wafer, as illustrated in figure 1b. Such systems will yield a significantly improved spatial resolution in remote sensing and a much greater antenna gain when implemented with phased arrays.

In our group, we are systematically investigating physical and engineering issues that are relevant to high-frequency and high-speed devices. Specifically, we are working on micromachined millimeter- and submillimeter-wave devices, far-infrared and picosecond time-resolved transport studies of lateral quantum-effect devices, and development of far-infrared lasers, photodetectors, and optical parametric amplifiers using multiple quantum-well structures.

3.2 Micromachined Millimeter-wave Devices

Sponsors

Defense Advanced Research Projects Agency
Contract MDA972-90-C-0021
National Aeronautics and Space Administration
Grant NAGW-4691
Grant 959705
National Science Foundation
Grant AST 94-23608

Project Staff

Dr. Gerhard de Lange, Arifur Rahman, Erik Duerr, Professor Qing Hu, Dr. Richard Ralston[1]

3.2.1 Micromachined Millimeter-wave SIS Receivers

Superconductor-insulator-superconductor (SIS) heterodyne receivers have been demonstrated to be the most sensitive receivers throughout 30-840 GHz frequency range. The challenge the in the SIS receiver technology is to extend their operating frequency into the THz range and to develop focal-plane arrays in order to improve the efficiency of data acquisition. In order to achieve these goals, we are currently developing a scheme to couple the millimeter-wave and submillimeter-wave signals to the superconducting devices by using a micromachined horn antenna and a planar antenna supported by a thin (~1 micron) membrane, as shown in figure 1a. As stated in the introduction, this novel micromachined antenna structure can be produced with a high precision using photolithography, and it can be utilized in focal-plane arrays, as shown in figure 1b.

Following our initial success in fabricating high-quality and high-current-density SIS junctions on free-standing SiN membranes, we have further improved our micromachining techniques for whole-wafer fabrication, higher yield, and better qualities side walls that are critical for the antenna performance. Recently, we have constructed and tested W-band (75-110 GHz) micromachined SIS receiver. Figure 2 shows the pumped I-V characteristic of an SIS receiver in a micromachined antenna structure. It also shows the response to a hot (the curved marked as 300 K) and a cold (at 77 K) blackbody

[1] Group 86, MIT Lincoln Laboratory.

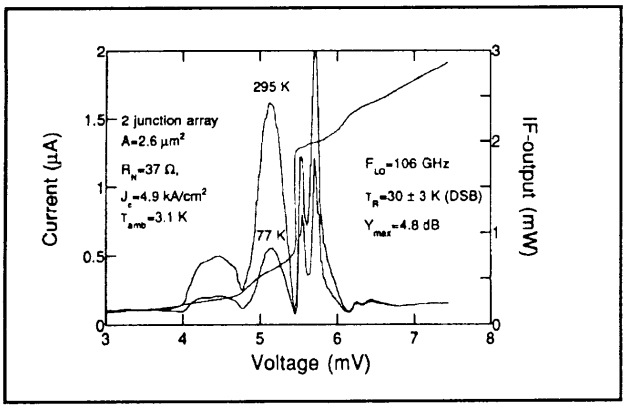

Figure 2. Pumped I-V characteristic of an SIS device in a micromachined antenna structure. The curve marked 300 K corresponds to the IF response when a hot (300 K) blackbody radiator is placed in front of the receiver, while the curve marked 77 K is with a cold load.

radiator at the intermediate frequency (IF). The 4.8-dB difference between the two curves corresponds to a double-sideband (DSB) noise temperature of 30 K (without any corrections). This result is comparable to the lowest receiver noise temperatures from the best waveguide systems that have been developed in the last 15 years. Our work has thus firmly established the micromachined receiver system as a competitive alternative to the conventional waveguide systems. We are currently designing and constructing 3×3 focal-plane array receivers using this technology, which should be tested in the coming year.

3.2.2 Micromachined Room-temperature Millimeter-wave Sensors

Due to a millimeter-wave's (especially around the 94-GHz atmospheric window) great penetration in foggy, dusty, and smoky environments and to its much better spatial resolutions compared to the longer wavelengths at microwave frequencies, sensitive room-temperature millimeter-wave devices are very useful in imaging and object identification and tracking. They are important for both military and commercial applications, such as motor vehicle collision avoidance radars. Based on our recent remarkable success in the development of micromachined SIS receivers, we are currently developing room-temperature millimeter-wave sensors using the micromachining technology.

We have used microbolometers (whose dimension is approximately several microns as illustrated in figure 3) in our micromachined systems. Microbolometers are easy to make (in fact, they are much easier to make than the superconducting tunnel junctions), robust, and sensitive. In addition, our micromachined millimeter-wave structure is ideal for bolometric detectors in such a way that the thin SiN membrane provides a natural thermal isolation that a sensitive bolometer requires.

The dominating noise source in bolometric detectors is the 1/f noise associate with the resistive element (which is usually made out of semimetal materials, such as Bi, to achieve a high resistance value for impedance matching). Recently, it was discovered in the field of superconducting electronics that a commonly used superconducting material, Nb, has an order of magnitude lower level of 1/f noise (at room-temperature) than Bi while still providing sufficiently high resistivity for impedance matching. Assuming we operate the microbolometers above the 1/f noise frequency region, the NEP (noise equivalent power) of the microbolometers is limited by the temperature fluctuation, i.e., the phonon noise. Using realistic parameters for thermal conductance, a room-temperature Nb microbolometer can achieve an NEP of 6×10^{-12} W/(Hz)$^{1/2}$. This is more than one order of magnitude lower than that of pyroelectric detectors, which are the commonly used room-temperature millimeter-wave sensors. This level of reduction in NEP will significantly improve the sensitivity of the detectors and reduce the required integration time by at least a factor of 100 for the same signal/noise ratio.

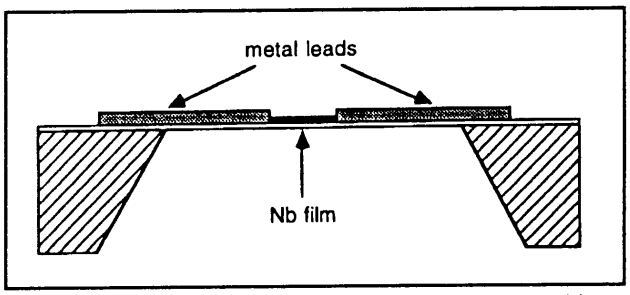

Figure 3. Schematic of a microbolometer supported by a thin membrane, which provides a good thermal insulation.

We have fabricated and tested several batches of Nb microbolometers with micromachined horn antennas. Figure 4 shows the speed and the noise performance of a microbolometer. Because of the low thermal mass associated with its small dimensions, a microbolometer has a roll-off frequency much higher than that of a conventional "macro" bolometer. This high speed may make the microbolometers useful in radar applications as well as in passive radiometry sensing. The left curve in figure 4 indicates the roll-off frequency of our microbolometer to be on the order of 10 kHz. The measured overall frequency dependence of the voltage responsivity agrees well with our theoretical calculations, which is shown as the dashed line. The noise equivalent power of this microbolometer is measured to be 4×10^{-10} W/Hz$^{1/2}$ at frequencies

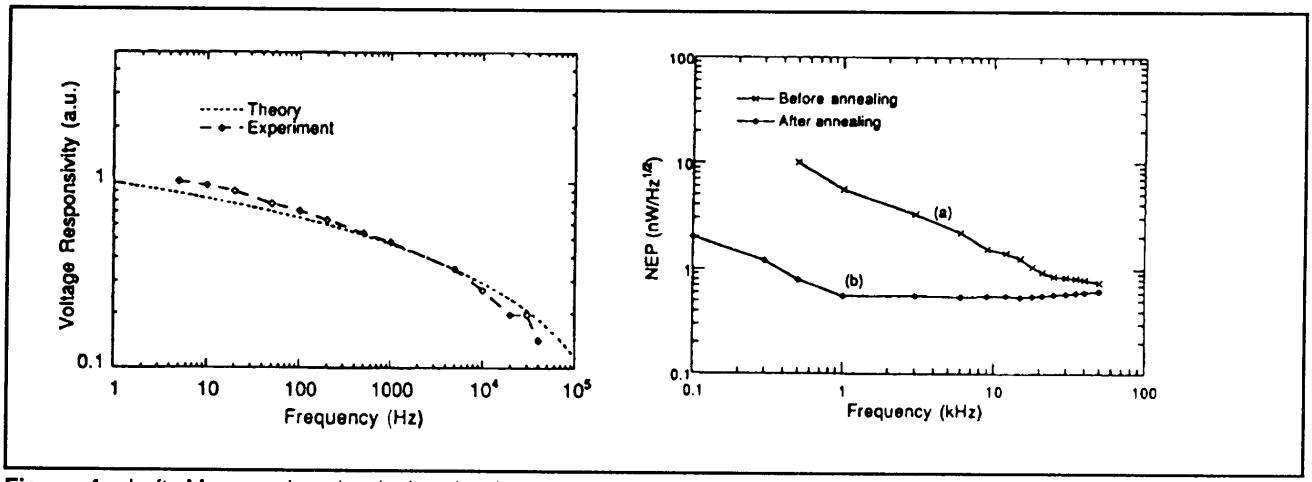

Figure 4. Left: Measured and calculated voltage responsivity as functions of the modulation frequency. Right: Noise equivalent power as a function of the frequency.

where the 1/f noise is not dominant. This result is already better than those for room-temperature pyroelectric detectors. With further improvements by optimizing the geometry of the SiN membrane, we should be able to reduce the NEP by another order of magnitude, which will make these microbolometers with micromachined antennas most sensitive uncooled millimeter-wave sensors.

3.3 Far-infrared and Picosecond Time-resolved Transport Studies of Quantum-effect Devices

3.3.1 Far-infrared Studies of Antenna-coupled Quantum Point Contacts

Sponsor

National Science Foundation/MRSEC
Grant DMR 94-00334

Project Staff

Rolf A. Wyss, Farhan Rana, Professor Qing Hu, Jésus A. del Alamo, Dr. Michael R. Melloch,[2] Dr. Michael J. Rooks[3]

Quantum transport has been one of the most active fields in solid-state physics in recent years. Advances in material preparation have made quantum phenomena profound in electron transport for many semiconductor quantum devices such as quantum point contacts, quantum dots, quantum wires, quantum wells, superlattices, etc. In clean samples and at low temperatures, electrons can travel through the whole sample without suffering phase-destructive scattering. Extensive work has been done to study various features of such phase-coherent quantum transport. However, most of the experiments reported so far are limited to measurements using dc transport and far-infrared spectroscopy.

It is well known in the field of superconducting tunneling that photons can assist the tunneling process, provided the tunneling is elastic. In a broad sense, elastic tunneling is a phase-coherent quantum transport process in a classically forbidden region. Therefore, all the results of photon-assisted tunneling can be applied to the study of photon-assisted quantum transport in semiconductor devices. This will provide a new dimension to study the exciting quantum transport phenomena. Novel long-wavelength optoelectronic devices may also emerge from this research.

In this project, we intend to study the interaction between far-infrared photons and ballistic electrons in quantum point contact devices. We have fabricated several antenna-coupled, quantum point contact devices using a combination of optical and electron-beam lithography. The dc transport measurement of the drain/source transport showed high quality of the devices. Under coherent far-infrared radiation at 285 GHz, a pronounced photon-induced drain/source current is produced throughout the

[2] Purdue University, West Lafayette, Indiana.

[3] Cornell National Nanofabrication Facility, Ithaca, New York.

gate voltage range in which the device exhibits the behavior of a one-dimensional electron system. This photon-induced current is attributed to a bolometric effect as described in the previous report.

In addition to the photoconductive effect, we have recently discovered a pronounced photovoltaic effect in several antenna-coupled quantum point contacts irradiated from 280 GHz to 2.5 THz. Figure 5a shows the drain/source current of an irradiated quantum poin contact *without* external drain/source bias. This induced current tracks the subband structure in a very regular manner that is similar to the transconductance of the device measured without radiation. We have identified this photovoltaic effect as a result of thermopower due to an asymmetric heating of the source and drain. This analysis is supported by experimental evidence that by shifting the focal spot of the radiation, we can reverse the polarity of the photon-induced current, as shown in figure 5.

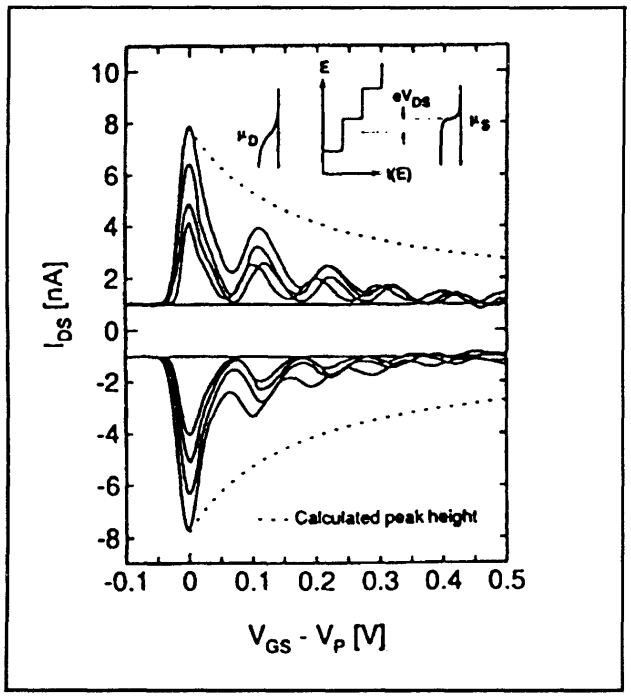

Figure 5. Measured photocurrents (at zero bias voltage) at different radiation power levels. (top) Positive currents correspond to beaming toward the source region, while (bottom) negative currents correspond to beaming toward the drain region.

3.3.2 Direct Simulation of Photon-assisted Transport

Sponsor

National Science Foundation/ MRSEC
Grant DMR 94-00334

Project Staff

Professor Qing Hu, Dr. Kou Yakubo,[4] Dr. Shechao Feng[4]

In spite of the straightforward analogy with the photoemission phenomenon, however, our experimental investigations have failed to provide evidence for photon-assisted transport. We have carried out extensive measurements over a broad frequency range from 90 GHz to 2.5 THz (corresponding to $\hbar\omega$ = 0.3 - 10 meV), with the radiation electric field polarization both along and perpendicular to the drain/source conductance path, which have yielded nothing but bolometric signals. It is natural to ask why such a simple process (which is analogous to so many well-established phenomena, such as photoemission in metals, photo-ionization of atoms, photon-excited bound-to-extended-state transitions in quantum-well structures, and photon-assisted tunneling in superconducting tunnel junctions) has not been observed in quantum-point-contact devices.

In this work, we solve time-dependent Schrödinger's equation numerically in order to investigate the conditions that could lead to a pronounced effect of photon-assisted transport. Our main finding is that the selection rule, which is the mathematical statement of the momentum conservation of the electron/photon systems, determines whether the electron transport is adiabatic or photon-excited. Mathematically, in order to achieve an appreciable photon-excited transition probability, the dipole-moment integration must be truncated to a region that is not much greater than the coherence length $1/\Delta k$, where Δk is equal to the momentum difference between the electrons before and after photon absorption/emission. This truncation can be achieved experimentally by either a localized electron state or a localized photon-field profile. Physically, this spatial localization of the electron or photon field provides the momentum spread that is necessary for the photon excitation process. Figure 6a shows a wave function (in k-space) in the presence of an ac field. The main peak at k = 0 corresponds to the wave function in a free space without radiation. The satellite peaks

[4] University of California, Los Angeles, California.

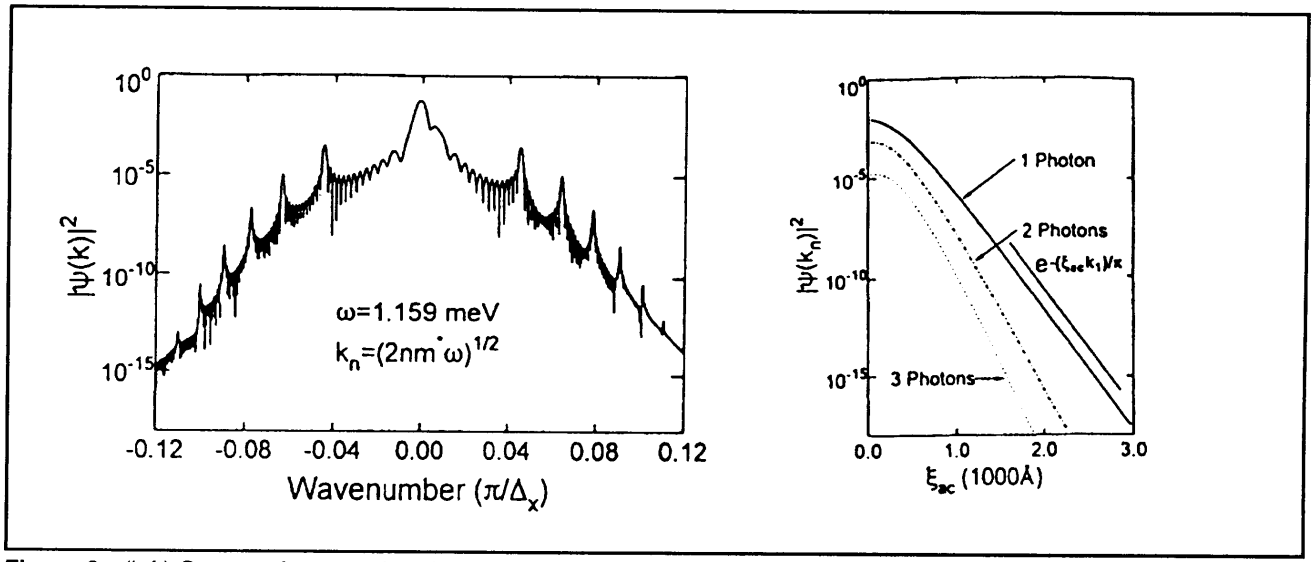

Figure 6. (left) Square of a wave function of free electrons (in k-space) under the irradiation of an ac field. The satellite peaks correspond to photon emission. (right) Values of photon-excited states as functions of the width of the ac field.

correspond to photon emissions. Figure 6b shows the amplitudes of these peaks as functions of the ac-field spatial width ξ_{ac}. Clearly, the photon-excitation process decreases exponentially as the ac-field spatial confinement loosens.

Our simulation indicates that the selection rule requires a spatially confined ac field if the photon-excited transition is between two extended electronic states, such as the case for quantum point contact devices. This can be achieved by bringing the antenna terminals very close to the central region. Photon excitation can also be achieved by using double- or multiple-barrier structures to create quasibound electronic states. The spatially localized nature of these quasibound states provide the momentum spread for the photon-assisted process. Our simulations have provided positive evidence to support this understanding.

The curve in figure 7 shows the enhanced transmission coefficient T* (defined as $(T_{ac} - T_{dc})/T_{dc}$, where T_{ac} is the transmission coefficient with a radiation field and T_{dc} is the one without) through a double-barrier structure as a function of the width of the ac field ξ_{ac}. In great contrast to the curve in figure 6, T* decreases algebraically with ξ_{ac}. This algebraic decrease is simply due to a decrease of the ac electric field strength in the active region between the two barriers as ξ_{ac} increases. This result differs qualitatively from that in figure 6, in which the interaction vanishes exponentially as ξ_{ac} increases because of the selection rule.

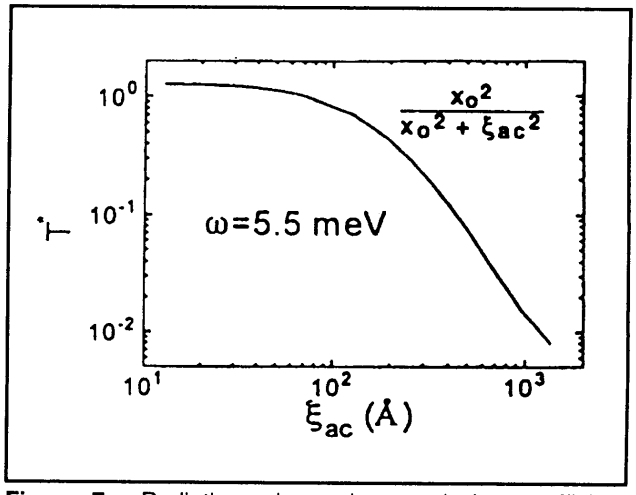

Figure 7. Radiation-enhanced transmission coefficient through an asymmetric double-barrier structure as a function of the width of an ac field ξ_{ac}. The parameters used in the simulation are: The left barrier has a height of 10.9 meV and width of 118 Å, the right barrier has a height of 12.2 meV and a width of 205 Å, the separation of the two barriers is 378 Å. The energy of the incident electrons is at the same level of the quasibound state at 9.2 meV, and the radiation frequency is 5.5 meV.

3.3.3 Photon-assisted Transport in Lateral Dual-gate Devices

Sponsors

MIT Lincoln Laboratory
Advanced Concept Program
Grant BX-5464
National Science Foundation/ MRSEC
Grant DMR 94-00334

Project Staff

Dr. Simon Verghese, Rolf A. Wyss, Dr. Thomas Schäpers, Professor Qing Hu, Arno Föster,[5] Dr. Michael J. Rooks[6]

As our direct simulation of photon-assisted transport indicates, photon absorption requires a momentum transfer of $\Delta k \sim m^*\omega/\hbar k_f$ for an electron with a wavevector $\sim k_f$ to absorb a photon with $k \sim 0$. This momentum transfer can be achieved by either localizing (1) the photon field to within the coherence length $1/\Delta k$, or (2) the electron wavefunctions. The devices described here supply Δk mainly by localizing the electron wavefunction in one dimension that is parallel to the photon's polarization. A similar scheme has been successfully implemented in mid-infrared ($\lambda \sim 10\ \mu m$) photon detectors using vertically grown quantum-well structures. These devices absorb photons when a 1D-localized electron in a bound state is excite into the continuum. In order to maintain a steady-state operation, the depleted electron in the quantum wells are supplied by thermionic electrons from the emitter over the barriers. In our case, the depleted electrons are supplied by tunneling injection from the source. Consequently, the eigenstates are quasibound states with lifetimes much greater than the modulation period of the ac field.

In figure 8b and 8c are shown the measured radiation-induced current as functions of the drain/source bias voltage V_{ds} (curves labeled by i). The two sets of curves are taken with radiation frequencies at 90 GHz (in b) and 270 GHz (in c). The radiation power level at both frequencies is approximately the same. It is very clear that the two sets of curves exhibit distinctively different features at the two radiation frequencies. The ones at 90 GHz show much sharper modulations of the radiation-induced current, while the ones at 270 GHz have much smoother features. This is due to the overlap of photon subbands at this high frequency, as illustrated in figure 8a. This frequency-dependent feature is the strongest evidence that the radiation-induced current is a photonic effect that depends on the energy of an individual photon. The curves labeled (ii) in figure 8b and 8c are calculated photocurrent based on the model of photon-assisted transport. They agree with the experimental results quite well. In comparison, the calculated radiation-induced current based on a bolometric model (labeled iv) is frequency independent and cannot explain the experimental results taken at 270 GHz.

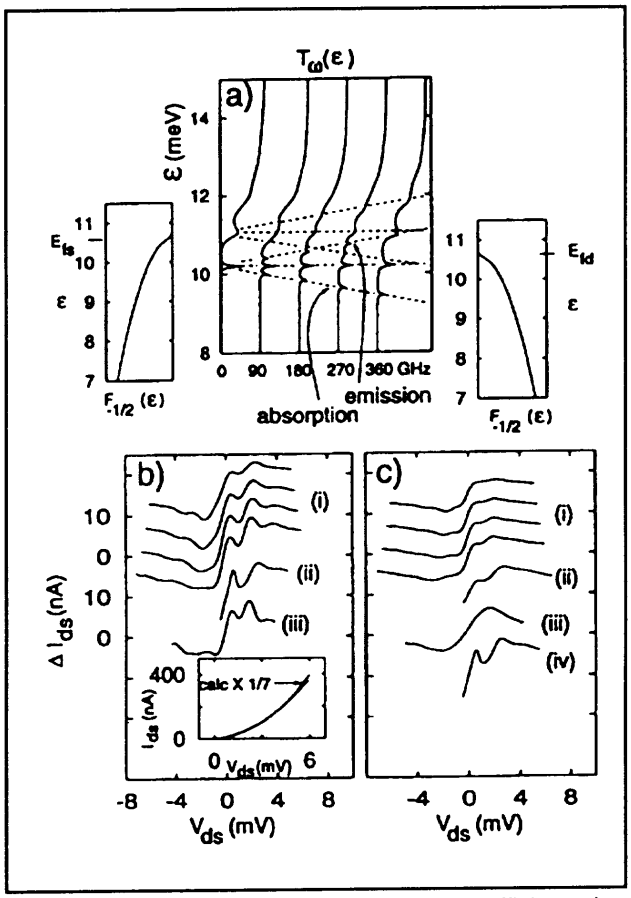

Figure 8. (a) Effective transmission coefficient that includes the effect of photon absorptions and emissions. (b) and (c) Curves (i): measured radiation-induced current at 90 GHz (b) and 27 GHz (c). Curves (ii): calculated radiation-induced current based on the model of photon-assisted transport. Curve (iv): calculated radiation-induced current based on heating model.

5 Forschungszentrum Jülich, Jülich, Germany.

6 Cornell National Nanofabrication Facility, Ithaca, New York.

3.3.4 Picosecond Dynamical Studies of Quantum-effect Devices

Sponsors

MIT Lincoln Laboratory
Advanced Concept Program
Grant BX-5464
National Science Foundation/MRSEC
Grant DMR 94-00334

Project Staff

Dr. Simon Verghese, Noah D. Zamdmer, Professor Qing Hu, Dr. Elliot Brown,[7] Dr. Michael R. Melloch,[8] Dr. Michael J. Rooks[9]

Modern solid-state physics and electrical engineering communities are witnessing a trend in which electronic devices are becoming smaller and faster. This is driven by modern society's insatiable appetite for an increased capacity of information processing and transmission. In this project, we use ultrafast probes to study the dynamics of ultrasmall devices.

We are pursuing two types of measurements. The first one involves a far-infrared spectrometer pumped by a mode-locked Ti:Sapphire laser which we recently constructed, as shown in figure 9. In this set up, two antenna-coupled Auston switches are pumped by a Ti:Al_2O_3 pulsed laser. The THz electrical pulses are launched into free space and then combined by a beam splitter. The combined beam is a superposition of two coherent subpicosecond electrical pulses whose relative time delay can be varied. These combined pulses will then be focused onto an antenna-coupled quantum device to generate a dc electrical current in the device through the photon-assisted transport/tunneling process. Effectively, the generated electrical current is proportional to the time autocorrelation function of the whole system, whose Fourier transform will give the frequency response of the system. We have constructed such a spectrometer and reported its THz performance in a previous report.

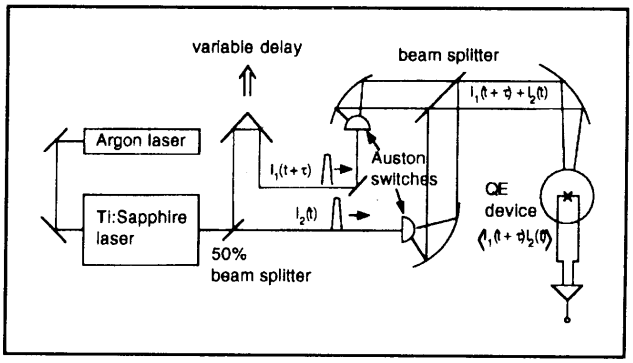

Figure 9. Schematic of an interferometer pumped by a pulsed Ti:Sapphire laser.

The second type of experiment involves a pump-and-probe method by integrating two Auston switches *monolithically* with the quantum-effect devices, as shown in figure 10. One switch will be used to apply a short electric pulse on the input, and the second one will be used to probe the output electrical current in a time-resolved fashion. This scheme differs from the first one in that the pump and probe beams are focused on *different* spots. In this way, we can measure the time scale of the transport process from the input to the output, as well as the spectroscopic information of the system. In order to achieve a high speed from the Auston switches, lattice-matched low-temperature-grown (LTG) GaAs materials will be used which have subpicosecond recombination time.

We have constructed a cryogenic system in which subpicosecond optical pulses are brought into the cryogenic stage through single-mode optical fibers. The schematic of this system, along with the measurement results, is shown in figure 11. The measurement shows the THz electrical pulse after propagating along a 2-mm long coplanar transmission line. Clearly, the signal-to-noise ratio improves as the temperature is lowered from the room temperature to 4.2 K. Also, the pulse width is reduced due to a lower loss of the transmission line at cryogenic temperatures. The time resolution of the current system is about five picosecond, which is mainly limited by the dispersion of the optical fibers. By using shorter fibers and longer optical pulses (picosecond instead of femtosecond) to minimize dispersion broadening), we are confident to be able to improve the time resolution to approximately one picosecond.

---

7 MIT Lincoln Laboratory, Lexington, Massachusetts.

8 Purdue University, West LaFayette, Indiana.

9 Cornell National Nanofabrication Facility, Ithaca, New York.

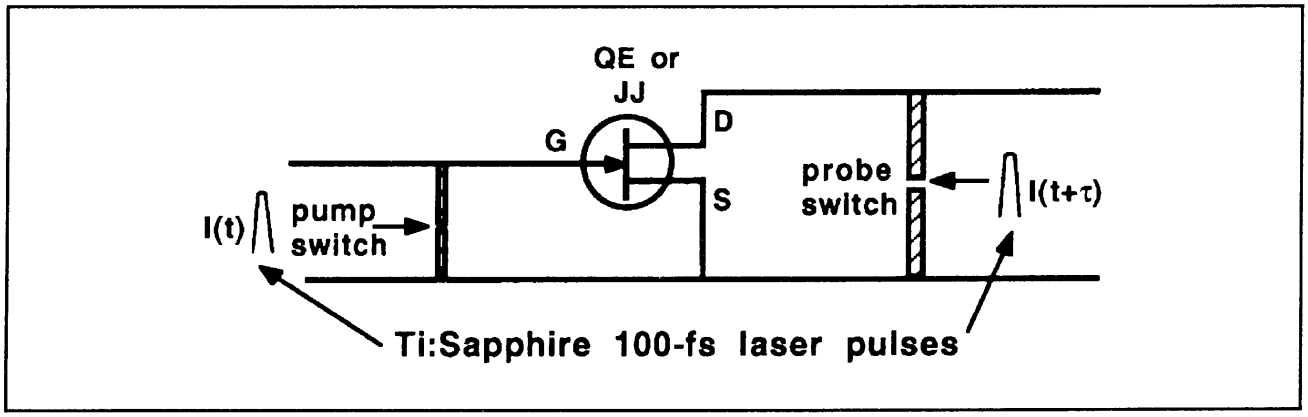

Figure 10. Schematic of a three-terminal (QE or Josephson) device pumped by a subpicosecond electrical pulse at the input, and the induced output current can be time-resolved by another time-delayed probe beam.

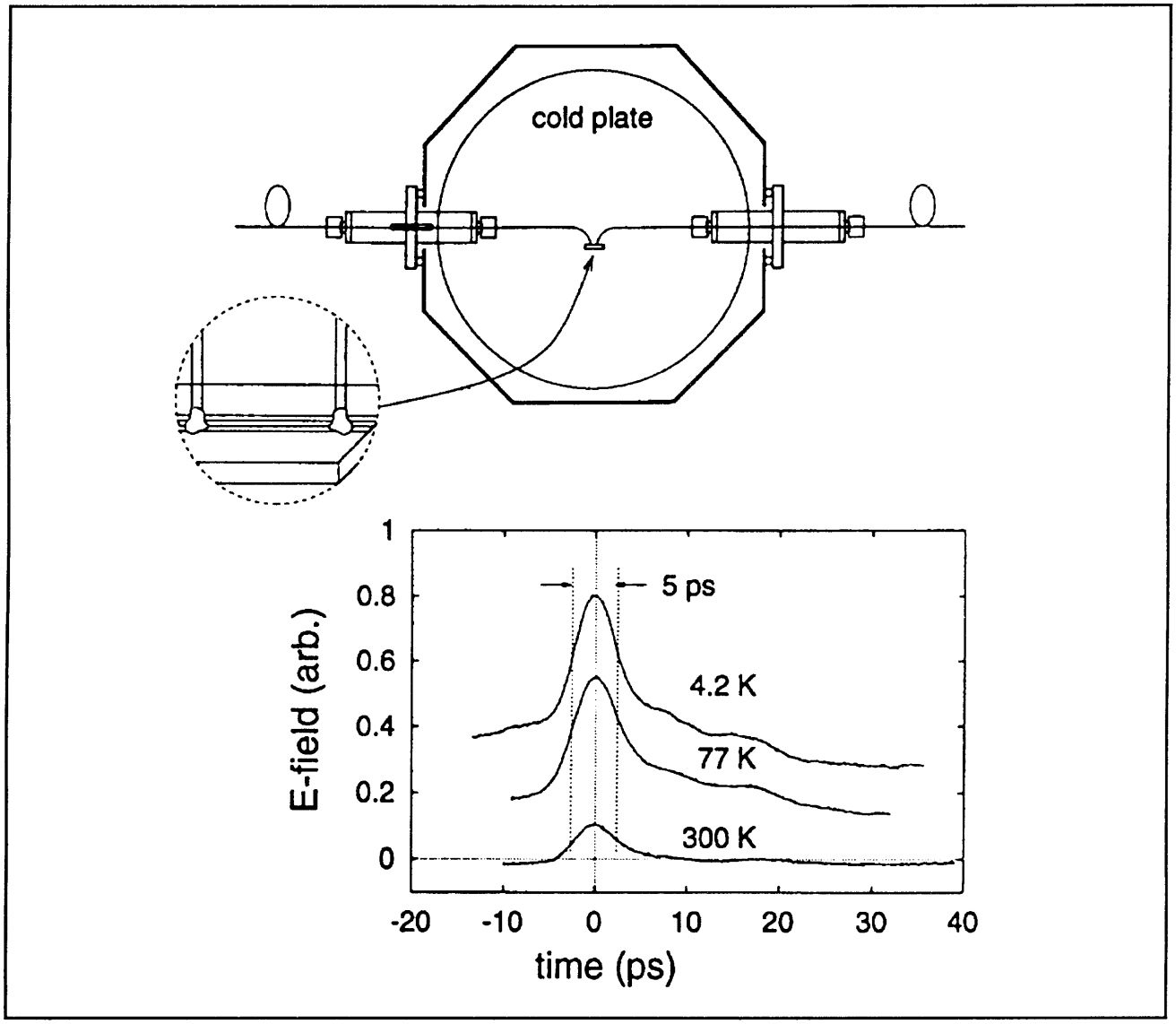

Figure 11. Top: Schematic of a fiber-coupled cryostat. Bottom: Time-resolved measurement of electrical pulses propagating through a 2-mm long coplanar transmission line.

3.3.5 Optical Correlators Using Low-temperature-grown GaAs (LTG) Photoconductors

During our investigation of picosecond time-resolved transport studies, we made an interesting discovery that may have potential applications in laser diagnostics and ranging. Since useful information is often contained in modulations of the intensity envelope of optical pulses, it is an important experimental task to measure the intensity-intensity autocorrelation function of the pulses $< I(t)I(t+\tau) >$. Traditionally, this is done by using a nonlinear crystal to double the frequency and then measure the autocorrelation function of the second harmonic. We have discovered that a photoconductor connected to a transmission line has a nonlinear response to the optical signal simply due to a voltage dividing between the photoconductor and the characteristic impedance Z_0 of the transmission line. This nonlinear response can be utilized to measure the second order correlation function $< I(t)I(t+\tau) >$. This concept is illustrated in figure 12a. Figure 12b shows the second-order nonlinear responsivity $S_I^{(2)}$ as a function of the incident power I(t). For the best contrast ratio, the incident power should be in the range that the photoconductance is comparable to $1/Z_0$. This corresponds to a power level of 0.01 mW, which is much lower than that required for conventional autocorrelators (typically >>1 mW). Since the LTG correlator does not require the use of a nonlinear crystal and all the components for phase matching, it is very compact, low cost, and sensitive. Figure 12c shows the measured results of fiber-broadened optical pulses (which preserve the spectral bandwidth). As the length of the fiber is increased, the pulse width increases noticeably as measured using our LTG correlator.

3.4 Intersubband Transitions in Coupled Multiple Quantum-well (MQW) Structures

Coupled MQWs are simply voltage tunable two-level or multilevel systems. Therefore, under specific bias conditions for carefully designed and fabricated MQWs, the devices can generate far-infrared radiation (when the initial state is higher than the final state), or detect far-infrared radiation (when the initial state is lower than the final state); or perform nonlinear optical functions such as parametric amplifications.

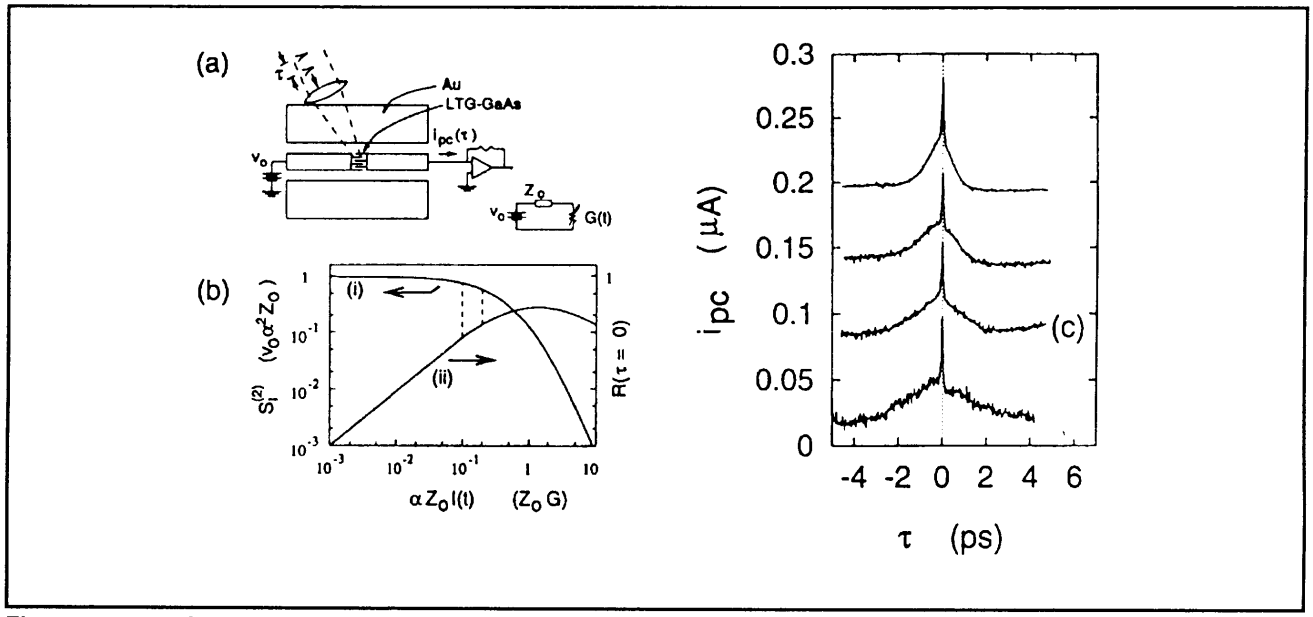

Figure 12. (a) Schematic diagram of the LTG-GaAs photoconductor embedded in a co-planar transmission line. The equivalent circuit models the high-frequency response of the LTG correlator to an intensity pulse I(t). (b) (i) Calculation of the second-order nonlinear current responsivity plotted in dimensionless units versus the normalized intensity $\alpha Z_0 I(t)$. (ii) Calculation of the contrast ratio plotted versus $\alpha Z_0 I(t)$. The shaded region indicates the optimum range of operation for the LTG correlator. (c) Output signal of the LTG correlator versus time delay τ for two optical pulses that were dispersed by propagating through 30, 50, 70, and 9 cm of fiber.

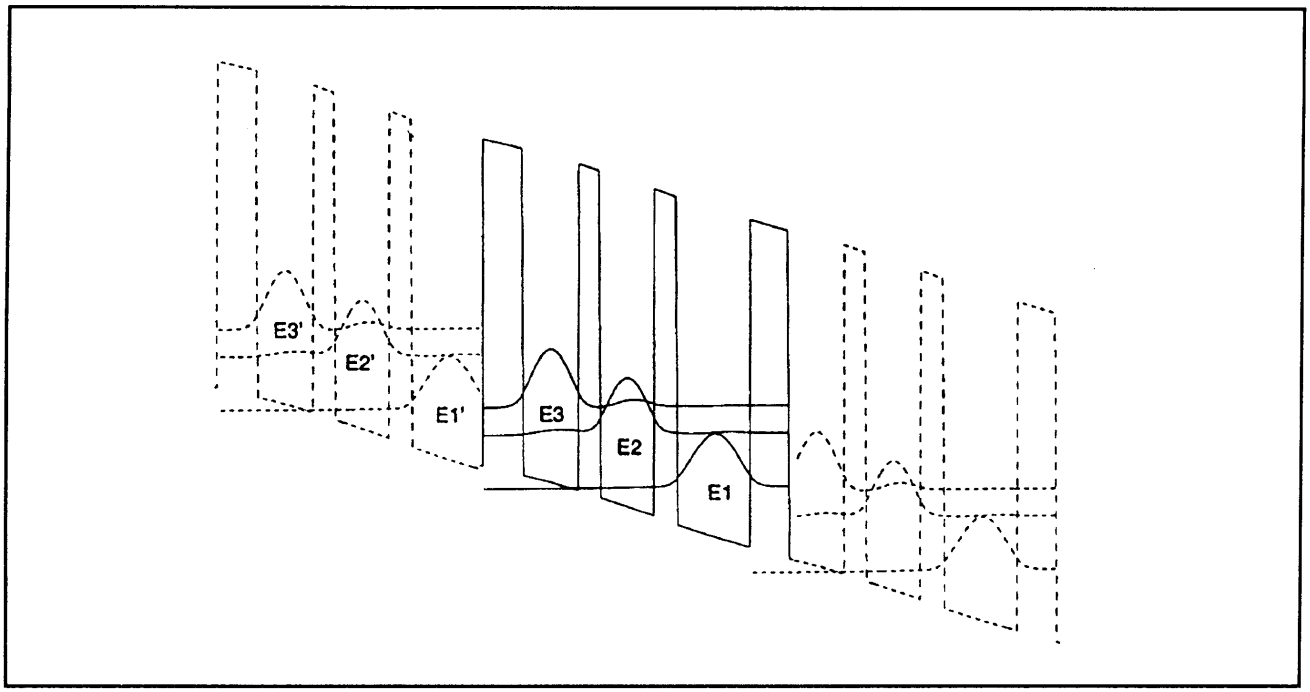

Figure 13. Conduction band profile and the square of wavefunctions for a MQW structure under the bias condition that the intersubband transition from E_3 to E_2 will generate radiation at 5 THz.

3.4.1 Far-infrared Lasers and Detectors Using MQW Structures

Sponsor

U.S. Army Research Office
Grant DAAH04-95-1-0610

Project Staff

Bin Xu, Professor Qing Hu, Dr. Michael R. Melloch[10]

The schematic of a single MQW module (sketched with solid lines) is shown in figure 13. The conduction band profile, subband structures, and carrier densities are calculated self-consistently from Schrödinger and Poisson equations, after typical five iterations. The lasing transition takes place between the subbands E_3 and E_2. The energy difference for this particular structure is designed to be 20 meV, which corresponds to 5 THz radiation frequency. The third quantum well on the collector side is used to improve injection efficiency by preventing electrons in E_3 to propagate to the collector. The energy difference between E_2 and E_1 is designed to be 36 meV, which is the LO phonon energy. Thus, the fast LO-phonon emission process will keep the E_2 level empty, maintaining an inverted population between E_3 and E_2. Our detailed calculation yields the following time scales for various relaxation processes: $\tau_{32} \sim 17$ ps (mainly due to electron-electron scattering), $\tau_{21} = 2.8$ ps (due to LO-phonon emission), and $\tau_{31} = 38$ ps (due to LO-phonon emission). These relaxation rates will easily produce an inverted population with an injection efficiency greater than 50 percent.

The most important parameter that determines the radiation properties (due to the 3→2 intersubband transition) of this MQW structure is the dipole moment $<3|z|2>$, or equivalently, the oscillator strength f_{32}, which is the ratio of the quantum mechanical radiative decay rate over that of a classical Hertzian dipole at the same frequency. We have chosen the barrier thickness that yields an oscillator strength of 0.25. This choice is made with a trade-off between a high oscillator strength and an acceptable rate of electron-electron scattering. With this design and by using 100 identical MQW modules (other modules are shown with the dashed lines in figure 13), the threshold carrier density will be approximately $3 \times 10^{10}/cm^2$. Consequently, lasing threshold can be reached at $e\Delta n/t_{32} \sim 1$ kA/cm^2 current density, which is quite feasible.

[10] Purdue University, West Lafayette, Indiana.

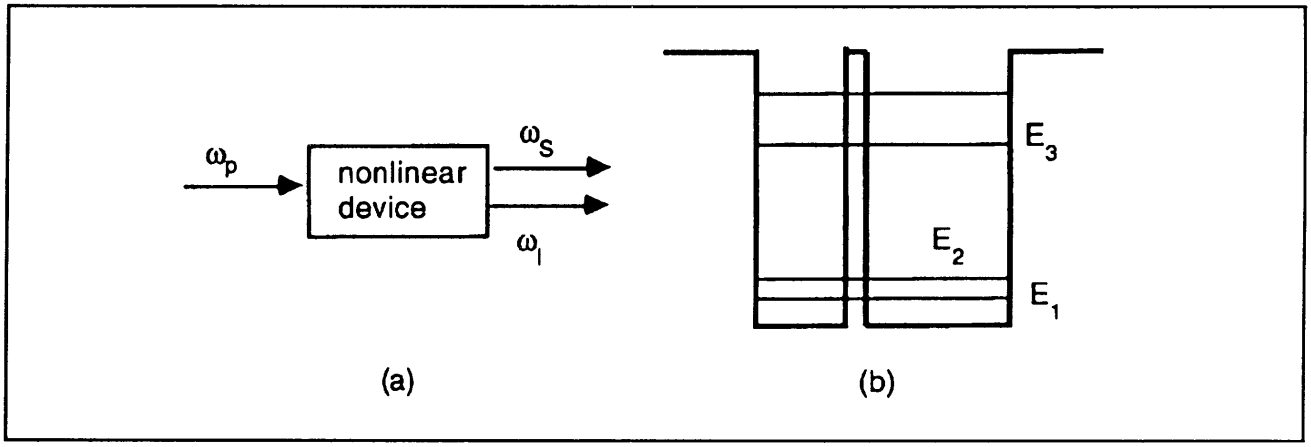

Figure 14. (a) Illustration of parametric amplification process, which converts a photon with a frequency ω_P into two photons with frequencies ω_i and ω_S, with $\omega_i + \omega_S = \omega_P$. (b) An asymmetric DQW structure that could produce a large $\chi^{(2)}$ at mid- and far-infrared frequencies.

3.4.2 Far-infrared Optical Parametric Amplifiers Using MQWs

Sponsors

Hertz Foundation Fellowship
U.S. Army - Office of Scientific Research
Grant DAAH04-94-G-0167

Project Staff

Ilya Lyubomirsky, Professor Qing Hu, Dr. Ben Streetman[11]

It is well known in the field of nonlinear optics that the nonlinear susceptibility $\chi^{(2)}$ is large near a resonant frequency for a system that is lack of inversion symmetry. Such a large $\chi^{(2)}$ has been widely used in second harmonic generation, second frequency generation, and parametric frequency down conversion at optical and near-infrared frequencies, where coherent sources at pump frequencies are readily available. As far as its optical properties are concerned, a quantum-well device acts like a giant atom, whose resonant frequencies are in the mid- to far-infrared frequencies. Naturally, if we design a QW structure so that it has resonances at mid-infrared frequency ($\lambda \sim 10$ microns) and far-infrared frequencies, we can use easily available CO_2 lasers as a pump source to parametrically generate far-infrared radiations. This nonlinear photon conversion process is illustrated in figure 14a.

However, a single quantum well has inversion symmetry, and therefore has a vanishing $\chi^{(2)}$. This problem can be solved easily by using a coupled DQW structure with asymmetric well widths, as shown in figure 14b. In this structure, the energy difference between levels 3 and level 1 is close to 120 meV (corresponding to a wavelength of 10 microns). This intersubband transition energy corresponds to the pump frequency. The energy difference between level 3 and 2 is approximately 20 meV, corresponding to the far-infrared signal frequency. The nonlinear susceptibility $\chi^{(2)}$ is proportional to the product of three dipole moments, $< z_{12} > < z_{13} > < z_{23} >$. By careful design, each dipole moment can be as large as several 10Å, which is at least one order of magnitude larger than that at optical frequencies for atomic systems. Using the doubly resonant structure shown in figure 14b, we estimate $\chi^{(2)}$ to be as large as 10^{-6} m/V, which is four orders of magnitude greater than the value for bulk GaAs materials. This extraordinarily large $\chi^{(2)}$ can be used for efficient parametric amplifications. The challenging issue of phase-matching can be solved by using Stark effect (changing the resonant conditions by applying a bias voltage) to control $\chi^{(2)}$ in selected regions to set up a periodic $\chi^{(2)}$, as shown in figure 15. In this structure, V_1 is tuned to be on resonance while V_2, off resonance. The length under the electrodes V_1 and V_2 are approximately one coherence length. This periodic nonlinear structure will provide conditions for quasi-phase-matching, thus approximately half of the total length will contribute to the parametric down conversion process.

[11] University of Texas, Austin, Texas.

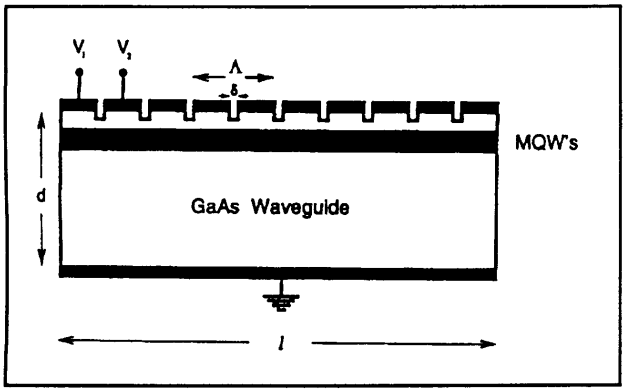

Figure 15. Periodic waveguide structure for quasi phase matching of the OPO.

3.5 Millimeter-wave, THz, and Subpicosecond Facilities

Professor Hu's laboratory is equipped with various millimeter-wave and infrared sources which can generate coherent and incoherent radiation from 75 GHz up to 30 THz. These include: Gunn oscillators at W-band frequencies (75-110 GHz); a frequency doubler, tripler, and quadrupler using Schottky diodes at 200, 300, and 400 GHz; an optically pumped far-infrared laser which generates coherent radiation from 245 GHz to 8 THz; and an infrared Fourier transform spectrometer which is capable in performing linear spectroscopy from 45 GHz to 30 THz and beyond. This laboratory is also equipped with various cryogenic millimeter-wave and infrared detectors. These include: Si composite bolometers, InSb hot-electron bolometers, superconductor-insulator-superconductor (SIS) receivers, and room-temperature microbolometers. Recently, with support from AT&T, a mode-locked Ti:sapphire laser that can generate optical pulses as short as 70 femtosecond was purchased and installed.

3.6 Publications

3.6.1 Journal Articles

de Lange, G., B.R. Jacobson, and Q. Hu. "A Low-noise Micromachined Millimeter-wave Heterodyne Mixer with Nb Superconducting Tunnel Junctions." *Appl. Phys. Lett.* Forthcoming.

de Lange, G., B.R. Jacobson, and Q. Hu. "Micromachined Millimeter-wave SIS Mixers." *IEEE Trans. Appl. Supercond.* 5: 1087 (1995).

Hu, Q., S. Verghese, R.A. Wyss, T. Schäpers, J. del Alamo, S. Feng, K. Yakubo, M.J. Rooks, M.R. Melloch, and A. Förster. "High-frequency (f ~ 1 THz) Studies of Quantum-effect Devices." Submitted to *Semicond. Sci. and Tech.*

Lyubomirsky, I., and Q. Hu. "Optical Parametric Oscillators Without Phasematching." Submitted to *Opt. Lett.*

Rahman, A., G. de Lange, and Q. Hu. "Micromachined Room-temperature Microbolometers for Millimeter-wave Detection." *Appl. Phys. Lett.* Forthcoming.

Smet, J.H., C.G. Fonstad, and Q. Hu. "Intrawell and Interwell Intersubband Transitions in Multiple Quantum Wells." Submitted to *J. Appl. Phys.*

Verghese, S., R.A. Wyss, T. Schäpers, A. Förster, M.J. Rooks, and Q. Hu. "Photon-assisted Transport Through Quantized Energy States in a Lateral Dual-gate Device." *Phys. Rev. B* 52: 14834 (1995).

Verghese, S., N. Zamdmer, E.R. Brown, A. Foerster, and Q. Hu. "An Optical Correlator using a Low-temperature-grown GaAs Photoconductor." Submitted to *Appl. Phys. Lett.*

Wyss, R.A., C.C. Eugster, J.A. del Alamo, Q. Hu, M.J. Rooks, and M.R. Melloch. "Far-infrared Radiation-induced Thermopower in a Quantum Point Contact." *Appl. Phys. Lett.* 66: 1144 (1995).

Yakubo, K., S. Feng, and Q. Hu. "Direct Simulation of Photon-assisted Quantum Transport." Submitted to *Phys. Rev. B.*

3.6.2 Conference Presentations

de Lange, G., B.R. Jacobson, and Q. Hu. "A Low-noise Micromachined Millimeter-wave Heterodyne Mixer with Nb Superconducting Tunnel Junctions." Paper published in the *Proceedings of the European Space Agency (ESA) Workshop on Millimeter Waves Technology and Applications,* Noordwijk, the Netherlands, December 1995, p. 231.

de Lange, G., B.R. Jacobson, A. Rahman, and Q. Hu. "Micromachined Millimeter-wave SIS Mixers." Paper published in the *Proceedings of the Sixth International THz Conference,* Pasadena, March 1995, p.372.

del Alamo, J.A., C.C. Eugster, Q. Hu, M.R. Melloch, and M.J. Rooks. "Electron Waveguide Devices." Invited paper published in the *Proceedings of the Eighth International Conference on*

Superlattices, Microstructures and Microdevices (ICSMM-8), Cincinnati, Ohio, August 1995. Forthcoming.

Hu, Q. "FIR Studies of Mesoscopic Devices." Invited paper presented at the *First Frontiers In Electronic Low-Dimensional Systems (FIELDS) Workshop on High Frequency Experiments on Low-Dimensional Systems,* Weizmann Institute of Science, Israel, November 1995.

Hu, Q. "High-frequency (f ~ THz) Studies of Quantum-effect Devices." Invited paper presented at *NATO Advanced Research Workshop on Future Trends in Microelectronics,* Ile de Bendor, France, July 1995.

Hu, Q., J. Smet, B. Xu, and I. Lyubomirsky. "Far-infrared (THz) Lasers and Parametric Oscillators Using Coupled Double Quantum-well Structures." Invited paper presented at the *International Conference on Intersubband Transitions in Quantum Wells: Physics and Applications,* Kibbutz Ginosar, Israel, October 1995.

Hu, Q., S. Verghese, R.A. Wyss, Schäpers, J. del Alamo, S. Feng, K. Yakubo, M.J. Rooks, M.R. Melloch, and A. Förster. "High-frequency (f ~ 1 THz) Studies of Quantum-effect Devices." Invited paper published in the *Proceedings of the International Semiconductor Device Research Symposium,* Charlottesville, Virginia, December 1995, p. 337.

Lyubomirsky, I., B. Xu, and Q. Hu. "THz Parametric Oscillators Using Coupled Double Quantum Wells." Paper publishedin the *Proceedings of the International Semiconductor Device Research Symposium,* Charlottesville, Virginia, December 1995, p. 623.

Rahman, A., G. de Lange, and Q. Hu. "Micromachined Room-temperature Microbolometers for Millimeter-wave Detection." Paper published in the *Proceedings of the International Semiconductor Device Research Symposium,* Charlottesville, Virginia, December 1995, p. 463.

Verghese, S., N. Zamdmer, E.R. Brown, A. Förster, and Q. Hu. "Correlation of Optical Pulses with a Low-Temperature-Grown GaAs Photoconductor." Paper published in the *Proceedings of the International Semiconductor Device Research Symposium,* Charlottesville, Virginia, December 1995, p. 433.

3.6.3 Patents

Verghese, S., E.R. Brown, and Q. Hu. "Low Temperature-Grown GaAs Correlator (LTGGC)." Filed for patent application, October 1995.

3.6.4 Thesis

Wyss, R.A. *Far-infrared Radiation Response of Antenna-coupled Quantum-effect Devices.* Ph.D. diss. Dept. of Elect. Eng. and Comput. Sci., MIT, 1995.